Constraints on the progenitor and explosion of SN 2024ggi in harmony with pre-explosion detection and hydrodynamic simulations

Amar Aryan $^{\textcircled{\scriptsize 0}}$, Erin Higgins $^{\textcircled{\scriptsize 0}}$, Matt Nicholl $^{\textcircled{\scriptsize 0}}$, Ting-Wan Chen $^{\textcircled{\scriptsize 0}}$, and Yu-Hsuan Liu $^{\textcircled{\scriptsize 0}}$

¹ Graduate Institute of Astronomy, National Central University, 300 Jhongda Road, 32001 Jhongli, Taiwan ² Astrophysics Research Centre, School of Mathematics and Physics, Queens University Belfast, Belfast BT7 1NN, UK

ABSTRACT

Supernova (SN) 2024ggi is a nearby Type II SN discovered by ATLAS, showing early flash-ionization features. The pre-explosion images reveal a red supergiant (RSG) progenitor with an initial mass of $10\text{--}17\,\mathrm{M}_{\odot}$. In the present work, we perform detailed hydrodynamic modeling to refine and put robust constraints on the progenitor and explosion parameters of SN 2024ggi. Among the progenitor models in our study, the pre-SN properties of the $11\,\mathrm{M}_{\odot}$ match the pre-explosion detected progenitor well. However, we find it difficult to completely rule out the $10\,\mathrm{M}_{\odot}$ and $12\,\mathrm{M}_{\odot}$ models. Thus, we provide a constraint of $11^{+1}_{-1}\,\mathrm{M}_{\odot}$ on the initial mass of the progenitor. To match the observed bolometric light curve and velocity evolution of SN 2024ggi, the favored model with an initial mass of $11\,\mathrm{M}_{\odot}$ has a pre-SN radius of $800\,\mathrm{R}_{\odot}$. This model requires an explosion energy of $[0.7\text{-}0.8]\times10^{51}\,\mathrm{erg}$, nickel mass of $0.049\,\mathrm{M}_{\odot}$, ejecta mass of $9.1\,\mathrm{M}_{\odot}$, and an amount of $\sim0.5\,\mathrm{M}_{\odot}$ of steady-wind CSM extended up to $\sim1.2\times10^{14}\,\mathrm{cm}$ resulting from an eruptive mass-loss rate of $1.0\,\mathrm{M}_{\odot}\,\mathrm{yr}^{-1}$. We also incorporate the accelerated-wind CSM scenario which suggests a mass-loss rate of $1.0\times10^{-2}\,\mathrm{M}_{\odot}\,\mathrm{yr}^{-1}$ and a CSM mass of $\sim0.7\,\mathrm{M}_{\odot}$ extended up to $\sim1.1\times10^{14}\,\mathrm{cm}$. This mass-loss rate falls within the range constrained observationally. Additionally, due to the constraint of $11^{+1}_{-1}\,\mathrm{M}_{\odot}$ on the initial mass, the range of pre-SN radius and ejecta mass would be $[690\text{-}900]\,\mathrm{R}_{\odot}$, and $[8.2\text{-}9.6]\,\mathrm{M}_{\odot}$, respectively.

Keywords: Stellar evolution (1599) — Red supergiant star (1375) — Type II Supernovae (1731)

1. INTRODUCTION

Followed by the discovery of the core-collapse supernova (CCSN) 2023ixf (K. Itagaki 2023) at a distance less than 10 Mpc (DLT10), another DLT10 CCSN 2024ggi was discovered in NGC 3621 by the Asteroid Terrestrial-impact Last Alert System (ATLAS) on the 11th of April 2024 (JD=2460411.64069, J. Tonry et al. 2024; S. Srivastav et al. 2024; T.-W. Chen et al. 2025) and it was classified as Type II (W. Hoogendam et al. 2024; Q. Zhai et al. 2024). Immediate spectroscopic follow-up starting only a few hours since discovery revealed the photoionized, optically-thick CSM surrounding the exploding star through the presence of strong, flash-ionization features in the spectra (W. V. Jacobson-Galán et al. 2024;

Corresponding author: A. Aryan

amararyan941@gmail.com, amar@astro.ncu.edu.tw

Corresponding author: T.-W. Chen

twchen@astro.ncu.edu.tw

T. Pessi et al. 2024; M. Shrestha et al. 2024; J. Zhang et al. 2024; T.-W. Chen et al. 2025).

Due to its proximity, the site of SN 2024ggi had been visited by numerous telescopes on several occasions before the explosion. Utilizing the pre-explosion images from the Hubble Space Telescope (HST) and the Spitzer Space Telescope, D. Xiang et al. (2024) identified a red, bright variable star with varying absolute F814W-band magnitudes of $-6.2\,\mathrm{mag}$ in 1995 to $-7.2\,\mathrm{mag}$ in 2003. The variation in F814W-band magnitudes was found consistent with a normal RSG star. For the identified progenitor, D. Xiang et al. (2024) constrained the temperature and bolometric luminosity to be $T_* = 3290^{+19}_{-27}\,\mathrm{K}$ and $\log(L/\mathrm{L}_\odot) = 4.92^{+0.05}_{-0.04}$, respectively.

In another study, X. Chen et al. (2024) examined the multi-band deep archival images in griz-bands from the Dark Energy Camera Legacy Survey, and provided the range of progenitor mass lying in 14– $17\,\mathrm{M}_{\odot}$. However, their progenitor mass estimation could be influenced by the flux contamination from a nearby source, as S. Srivastav et al. (2024) had indicated that the red source was

resolved into two sources in F814W-band image from HST. S. Yang et al. (2024) also measured the brightness at the location of SN 2024ggi in the DESI Legacy Survey images and found absolute magnitudes within the range typical for an RSG. Further utilizing the HST images, X. Hong et al. (2024) put constraints on the progenitor mass through independent measurements unaffected by the circumstellar extinction and pulsational brightness variability. They found the dying star associated with the youngest population in SN environment with an age $(\log[t/yr])$ of 7.41, corresponding to an initial mass of $10.2^{+0.06}_{-0.09}\,\mathrm{M}_{\odot}$.

Despite some constraints over the progenitor masses through the direct detection of the possible progenitor in pre-explosion images, detailed hydrodynamic simulations are **scarce** in the literature to strengthen the claims on the progenitor star and explosion properties. However, K. Ertini et al. (2025) utilized a grid of progenitor models available from K. Nomoto & M. Hashimoto (1988) to reproduce the observed bolometric light curve and velocity evolution of SN 2024ggi. They constrained an initial progenitor mass of $15\,\mathrm{M}_\odot$.

In the present study, we performed detailed hydrodynamic simulations of the possible progenitor models and constrained the explosion properties of the exploding star. The rest of the paper is organized as follows. Section 2 details the numerical setups to generate several progenitor models with different zero-age main-sequence (ZAMS) masses and evolve them up to the pre-SN stages. Section 3 details the explosion setups to mimic the SN 2024ggi properties, thus putting important constraints on the explosion and circumstellar properties. Finally, in Section 4, we summarize our key findings and implications of our analysis on putting the constraints over the progenitor and explosion properties of SN 2024ggi.

$\begin{array}{c} \text{2. CONSTRAINTS ON THE POSSIBLE} \\ \text{PROGENITOR} \end{array}$

As seen above, initially, the direct detection of the possible progenitor in the pre-explosion images put a constraint of $13-17\,\mathrm{M}_\odot$ (D. Xiang et al. 2024; X. Chen et al. 2024) on the progenitor mass. However, an environmental analysis (free from the effect of circumstellar extinction and pulsational brightness variability) by X. Hong et al. (2024) utilizing the pre-explosion HST images of SN 2024ggi site, places the progenitor towards the slightly lower mass regime. As a result, we choose $[10-17]\,\mathrm{M}_\odot$, ZAMS star models in our simulations to serve as the possible progenitor for SN 2024ggi.

$\begin{array}{ccc} 2.1. & Details \ on \ simulation \ setups \ to \ create \ pre\text{-}SN \\ & models \end{array}$

Starting from the pre-main-sequence, our models arrive on the ZAMS with specified masses and respective rotations, pass through stages of successive nuclear burning and finally reach the pre-SN stages marked by the Iron-core (Fe-core) infall. To evolve the models upto the stages of Fe-core infall, we employ the state-of-theart simulation tool MESA, version r24.03.1 (B. Paxton et al. 2011, 2013, 2015, 2018, 2019; A. S. Jermyn et al. 2023). Our models have solar metallicity (Z = 0.0142, following M. Asplund et al. 2009) and nominal rotation, which is only the 5% of their critical angular rotational velocity. The solar metallicity composition for SN 2024ggi progenitor is supported by W. V. Jacobson-Galán et al. (2024); D. Xiang et al. (2024); X. Chen et al. (2024); T.-W. Chen et al. (2025); X. Hong et al. (2024). The nominal angular rotation velocity of only 5% of their critical angular rotational velocity is supported by the fact that the progenitors of Type IIP SNe are RSGs (confirmed through direct detection of progenitors, e.g., S. J. Smartt 2009; S. D. Van Dyk 2017) that are typically very slow or non rotating due to their extended envelope (A. Heger & N. Langer 1998; A. Maeder & G. Meynet 2001).

We use the 12M_pre_ms_to_core_collapse test-suite directory of MESA to create the pre-SN models. As specified in the recent versions of MESA setups, when the hydrogen mass fraction in the core decreases to 0.68, the model is assumed to have reached the ZAMS stage (previously, the ratio of energy produced from nuclear reactions and the overall luminosity of the model being ~ 0.4 –0.8 was used to define the arrival on ZAMS). In our models, convection is modeled following the mixing theory of L. Henvey et al. (1965), adopting the Ledoux criterion. We have adopted a mixing-length-theory parameter ($\alpha_{\rm MLT}$) = 2.0 (typical value being $\sim 1-3$, as used in R. Farmer et al. 2016; A. Aryan et al. 2021; R. Ouchi & K. Maeda 2021; S. B. Pandey et al. 2021; A. Aryan et al. 2022c,b,a, 2023; A. K. Ror et al. 2024). Following N. Langer et al. (1985), semi-convection is incorporated in our models with an efficiency parameter of $\alpha_{\rm sc} = 0.01$. To model the convective overshooting, we use the default MESA settings for massive stars by setting overshooting parameters, f = 0.345 and $f_0 = 0.01$ for the hydrogen core, assuming step overshooting. The choice of step overshooting for the hydrogen core in massive stars introduces a sharp boundary extension that ultimately helps capture the increased main-sequence lifetime and observed main-sequence width. The chosen value of fand f_0 using step overshooting for hydrogen core are supported by I. Brott et al. (2011) and also by asteroseis-

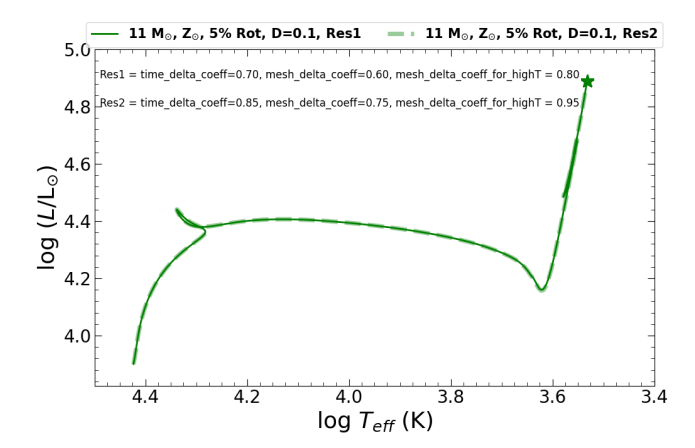


Figure 1. The stellar evolutionary tracks (from ZAMS to pre-SN stage) of $11 \, \mathrm{M}_{\odot}$ progenitor models in our simulations, assuming two sets of temporal and spatial resolutions. The models seem to have converged for the chosen temporal and spatial resolutions.

mology results around this mass range (D. M. Bowman 2020). The helium core would be relatively smaller, less vigorous, and the overshoot-induced mixing is expected to decay with distance. Thus, we use f = 0.01 and $f_0 = 0.005$ for helium core assuming exponential overshooting utilizing the results of F. Herwig (2000). In addition to these convective core overshooting, we also use a small amount of overshooting on the top of any other convective core to avoid spurious numerical behavior. The RSGs retain most of their outer envelope; thus, we use the 'Dutch' wind scheme (E. Glebbeek et al. 2009) with scaling factor (η) of 0.1 only, which accounts for the small mass losses. This wind scheme incorporates the outcomes from multiple works for different situations; (a) in the regions with the effective temperature, $T_{\rm eff} > 10^4 \, \rm K$ along with hydrogen mass fraction > 0.4, the outcomes of J. S. Vink et al. (2001) are used; (b) when $T_{\rm eff} > 10^4 \, \rm K$ and hydrogen mass fraction < 0.4, the results of T. Nugis & H. J. G. L. M. Lamers (2000) are used; and (c) the wind scheme presented in C. de Jager et al. (1988) is used for the regions with $T_{\rm eff} < 10^4 \, \rm K$. Throughout the simulation, we use appropriate temporal and spatial resolution. Figure 1 displays the effect of changing the temporal and spatial resolutions for the $11 \,\mathrm{M}_{\odot}$, thus confirming the convergence of our model grid within the assumed resolutions in our study.

With these settings, we evolve the models up to the pre-SN stages, marked by the infall velocity of any region inside the Fe-core exceeding 1000 km s⁻¹. In other words, the pre-SN stages in our simulations mark the onset of core collapse.

2.2. Discussion on the choice of η and rotation

The progenitors of Type IIP SNe are RSGs with their outer hydrogen envelope almost intact. We have assumed a small $\eta = 0.1$ to account for the low mass-loss rates. There are examples (e.g., B. Paxton et al. 2018) where an $\eta = 0.1$ has helped to produce the desired amounts of hydrogen and ejecta masses to explain the observed plateau durations of Type IIP SNe. In Figure 2, we see that changing η from 0.1 to 0.2 for the $11 \,\mathrm{M}_{\odot}$ (and also $15 \,\mathrm{M}_{\odot}$) has a negligible effect on the overall evolution of the star. Their physical properties at different stages of evolution are also almost identical, as presented in Table 1. Additionally, it is argued that RSG mass-loss rates may be much lower than the 'Dutch' prescription (E. R. Beasor et al. 2020). We also refer to J. T. van Loon (2025) for a review on RSG mass losses, which supports the typically modest rates of mass loss for progenitors of SNe IIP, compared to those of more massive red supergiants. Further, while modeling the light curves of SN 2004A, SN 2004et, SN 2009ib, SN 2017eaw, and SN 2017gmr, J. A. Goldberg & L. Bildsten (2020) found several models with $\eta = 0.2$ explaining the bolometric light curves and velocity evolution nicely. We also investigate the effect of changing η to 1. One important thing to notice in Figure 2 is that the terminating positions of the models with different η on the HR-diagram do not change considerably, as shown by the $11 \,\mathrm{M}_{\odot}$ and $17 \,\mathrm{M}_{\odot}$ models. However, due to an increased η , the pre-SN mass changes considerably as presented in Table 1.

Rotation in stars is a natural consequence of angular momentum conservation during the gravitational collapse of a star-forming molecular cloud. Virtually all stars rotate, although the rotation rate varies widely depending on physical characteristics like mass, age, metallicity, magnetic braking, and evolutionary stage. Several studies have shown that including rotation in stellar evolution models helps to explain the observed surface chemical enrichment, extended lifetimes, position on HR-diagram, and pre-SN core masses (among several others, A. Maeder & G. Meynet 2000; I. Hunter et al. 2008; C. Georgy et al. 2013). As indicated by S. Ekström et al. (2012), for the stars with initial mass range in $9-20\,\mathrm{M}_{\odot}$, the surface rotation velocities after the end of their respective core carbon burning stages are virtually close to zero. In the present study, we choose an initial angular rotational velocity of only 5% of the critical angular rotational velocity. As expected, the final surface velocities in our models are exceptionally low ($\sim 0.02 \text{ km s}^{-1}$ for the $11 \, \mathrm{M}_{\odot}$). We also show the non-rotating model for the $11\,\mathrm{M}_\odot$ and find that its evolution is almost identical to the slow rotating case



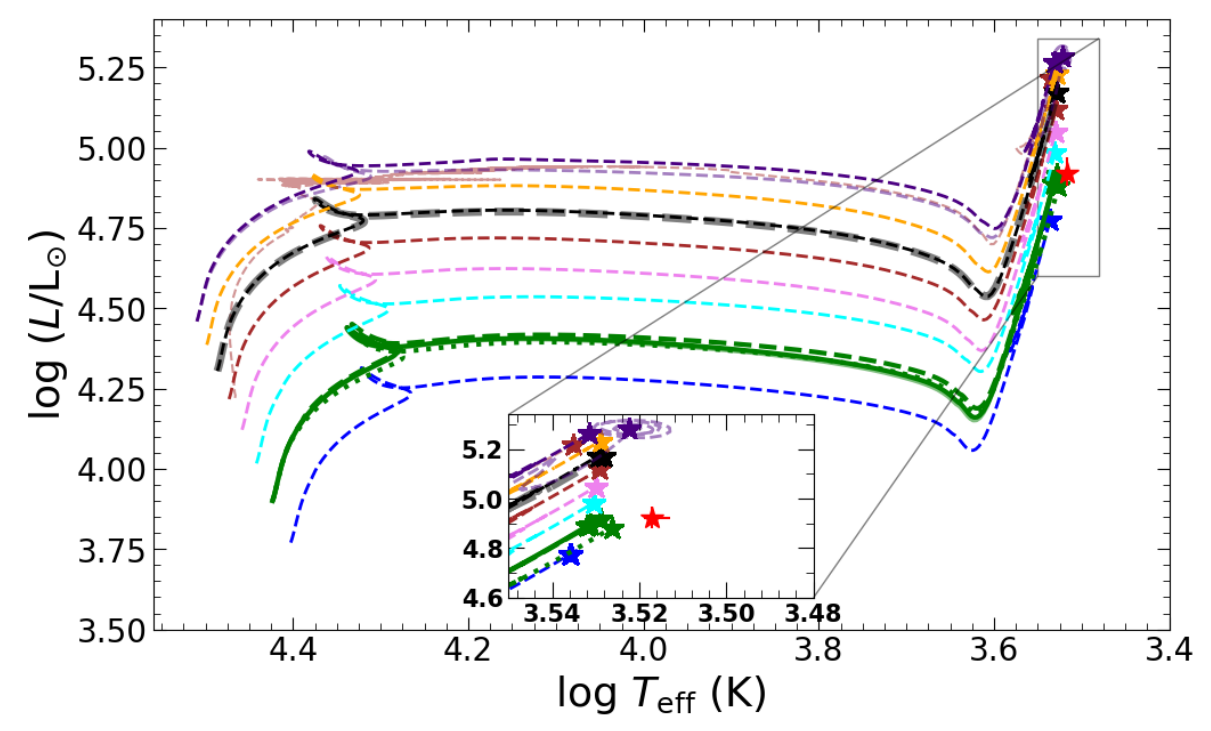


Figure 2. The evolutionary tracks of 10, 11, 12, 13, 14, 15, 16, and 17 M_{\odot} progenitor models in our simulations. The tracks shown here start from ZAMS and terminate at the pre-SN stages marked by ★ for each model. The location of the HST-detected progenitor candidate is also indicated (from D. Xiang et al. 2024). The inset shows our models' zoomed late stages of evolution.

(i.e., 5% Rot case) within the limits of the considered temporal and spatial resolutions here. One can argue for choosing high initial angular rotational velocities, however, as shown for the $14\,\rm M_{\odot}$ in Figure 2, increasing the initial angular rotational velocity from 5% to 40% significantly alters the overall evolution of the models. A critical consequence of increasing the initial rotation would be that the terminating stages of the models with high initial masses would move further away on the HR-diagram from the pre-explosion detected progenitor. Thus, a rapidly rotating high-mass progenitor would be less favored for SN 2024ggi.

2.3. Constrain on the physical properties of the possible progenitor

The evolutionary tracks of the models shown in Figure 2 start from ZAMS and terminate at their respective pre-SN stages marked by \bigstar for each model. The position of the **possible** progenitor detected in the pre-explosion images from HST (results from D. Xiang et al.

2024) is also indicated. The effective temperature $T_{\rm eff}$, and luminosity $\log(L/{\rm L}_{\odot})$ of the 11 ${\rm M}_{\odot}$ model at pre-SN stage seems to align well with the progenitor candidate directly detected from HST in archival images. At the pre-SN stage, the 11 ${\rm M}_{\odot}$ model has a radius of 800 ${\rm R}_{\odot}$. Additionally, the age ($\log[t/{\rm yr}]$) of the 11 ${\rm M}_{\odot}$ model at the pre-SN stage is 7.38, matching closely with X. Hong et al. (2024).

Although the pre-SN properties of $11\,\mathrm{M}_\odot$ model seems to match the physical properties of the **possible** progenitor detected in pre-explosion images, it is difficult to completely rule out the $10\,\mathrm{M}_\odot$ and $12\,\mathrm{M}_\odot$ models. These models have pre-SN radii of $690\,\mathrm{R}_\odot$ and $900\,\mathrm{R}_\odot$, respectively. Thus, for the progenitor of SN 2024ggi, we provide a constrain of $11^{+1}_{-1}\,\mathrm{M}_\odot$ on the initial mass, and a range of pre-SN radius of $690\,\mathrm{R}_\odot$ – $900\,\mathrm{R}_\odot$. These constraints align nicely with the values obtained by analyzing the pre-explosion images (as in D. Xiang et al. 2024; X. Hong et al. 2024). The error bar on our initial mass constraint represents the range of masses lying in

Table 1. The ZAMS and pre-SN properties of progenitor models using MESA along with the STELLA explosion parameters.

	ZAMS					Pre-SN			Explosion		
$M_{ m ZAMS}^a$	$T_{ m eff}$	R_{ZAMS}^{b}	$\log L_{\mathrm{ZAMS}}^{c}/\mathrm{L}_{\odot}$	$M_{\rm pre-SN}^d$	$T_{ m eff}$	$R_{\text{pre-SN}}^e$	$\log L_{\rm pre-SN}^f/{\rm L}_{\odot}$	M_{cf}^{g}	$M_{\rm ej}^h$	$M_{ m Ni}^i$	E_{exp}^{j}
$({ m M}_{\odot})$	K	$({ m R}_{\odot})$		$({ m M}_{\odot})$	K	$({ m R}_{\odot})$		$({ m M}_{\odot})$	$({ m M}_{\odot})$	$({\rm M}_{\odot})$	(10^{51} erg)
10.0	25300	4.0	3.77	9.9	3450	690	4.78	1.68	8.2	0.049	0.7
11.0^{\dagger}	26500	4.2	3.90	10.8	3400	800	4.89	-	_	-	-
11.0	26500	4.2	3.90	10.8	3400	800	4.89	1.71	9.1	0.049	0.7
11.0^{*}	26500	4.2	3.90	10.6	3400	840	4.92	1.71	8.9	0.049	0.7
11.0**	26500	4.2	3.90	9.5	3400	820	4.88	1.68	7.8	0.049	0.7
12.0	27700	4.4	4.02	11.8	3390	900	4.98	2.17	9.6	0.049	0.7
13.0	28700	4.6	4.12	12.7	3390	970	5.05	2.47	10.2	0.049	0.7
14.0	29700	4.8	4.22	13.6	3380	1060	5.12	1.95	11.7	0.049	0.7
14.0^{\ddagger}	29300	5.0	4.22	13.4	3400	1150	5.22	_	_	_	_
15.0	30700	5.0	4.30	14.5	3380	1120	5.17	-	_	-	-
15.0^{*}	30700	5.0	4.30	14.1	3370	1130	5.17	_	_	_	_
16.0	31500	5.2	4.38	15.4	3380	1200	5.23	-	_	-	-
17.0	32400	5.4	4.46	16.5	3400	1240	5.27	-	_	-	_
17.0**	32400	5.4	4.46	10.1	3330	1310	5.28	_	-	_	_
Additi	onal model	s: $11~{ m M}_{\odot}$	with fixed $M_{\rm Ni}=$	$0.049\mathrm{M}_\odot$ an	d differ	ent $E_{\rm exp}$					
								1.73	9.1	0.049	0.6
								1.69	9.1	0.049	0.8
Addition	al models:	$11~{\rm M}_{\odot}$ wi	th fixed $E_{exp}=0$.	7×10^{51} erg	and diff	erent M_{Ni}					
								1.71	9.1	0.035	0.7
								1.71	9.1	0.045	0.7
								1.71	9.1	0.049	0.7
								1.71	9.1	0.055	0.7
								1.71	9.1	0.065	0.7

^a Mass at ZAMS. ^bProgenitor radius at ZAMS, ^cLuminosity at ZAMS, ^dFinal mass at the pre-SN stage, ^ePre-SN phase radius, ^fPre-SN phase luminosity, ^gFinal core mass after fallback, ^hEjecta mass, ⁱAmount of synthesized Nickel, ^jtotal energy after explosion energy. [†] The non-rotating case. The properties of the non-rotating $11\,\mathrm{M}_{\odot}$ model are indistinguishable with the slowly rotating model within the limits of resolutions considered here. It's explosion results are expected to be almost similar as the slow rotating case (i.e., similar to Rot 5% case). * With $\eta = 0.2$. ** With $\eta = 1$. [‡] With initial angular rotation velocity of 40% of critical angular rotation velocity. Unless mentioned, $\eta = 0.1$ is used. All the MESA-inlist-files, pre-SN models, STELLA input files to generate luminosity, velocity evolution, and also the final STELLA result files, are available on Zenodo, MESA community and also on Zenodo, AAS Journals community.

the closest vicinity of the error bar of the pre-explosion detected progenitor on the HR-diagram. The details of the physical properties of the models at different stages are provided in Table 1.

3. CONSTRAINTS ON THE EXPLOSION PROPERTIES

In the previous section, we explored the physical properties of the models at their pre-SN stages marked by the onset of Fe-core infall. Next, the models are allowed to continue evolving until they reach near-shock breakout (SBO) stages utilizing the ccsn_IIp test-suite directory of MESA. The pre-SN model from the 12M_pre_ms_to_core_collapse directory is incorporated as the starting point in the ccsn_IIp test-suite directory. In this test-suite directory, the central region of the model where the entropy per baryon reaches $4\,k_{\rm B}$, is first removed. This excision represents the part of the model that would have collapsed to form a proto-

neutron star. The model is further allowed to continue infalling until its inner boundary (IB) reaches close to the location of the stalled shock. After the first few seconds, we account for further fallback by removing negative velocity material at the IB. The explosion is simulated by injecting energy in a thin layer of approximately $0.2 \,\mathrm{M}_{\odot}$ at the IB for $0.2 \,\mathrm{seconds}$, at a rate sufficient enough to raise the total energy of the model to our specified value of $E_{\rm exp}$. We also set the amount of nickel (M_{N_i}) synthesized in the SN. The mass of the SN ejecta (M_{ej}) is determined by subtracting the final core mass after fallback (M_{cf}) from the mass of the progenitor model at pre-SN stage $(M_{\text{pre-SN}})$. Thus, $M_{\text{ej}} =$ $M_{\rm pre-SN}$ - $M_{\rm cf}$. The detailed explanation of how the models are simulated from Fe-core infall till near SBO stages is documented in Section 6.1 of B. Paxton et al. (2018).

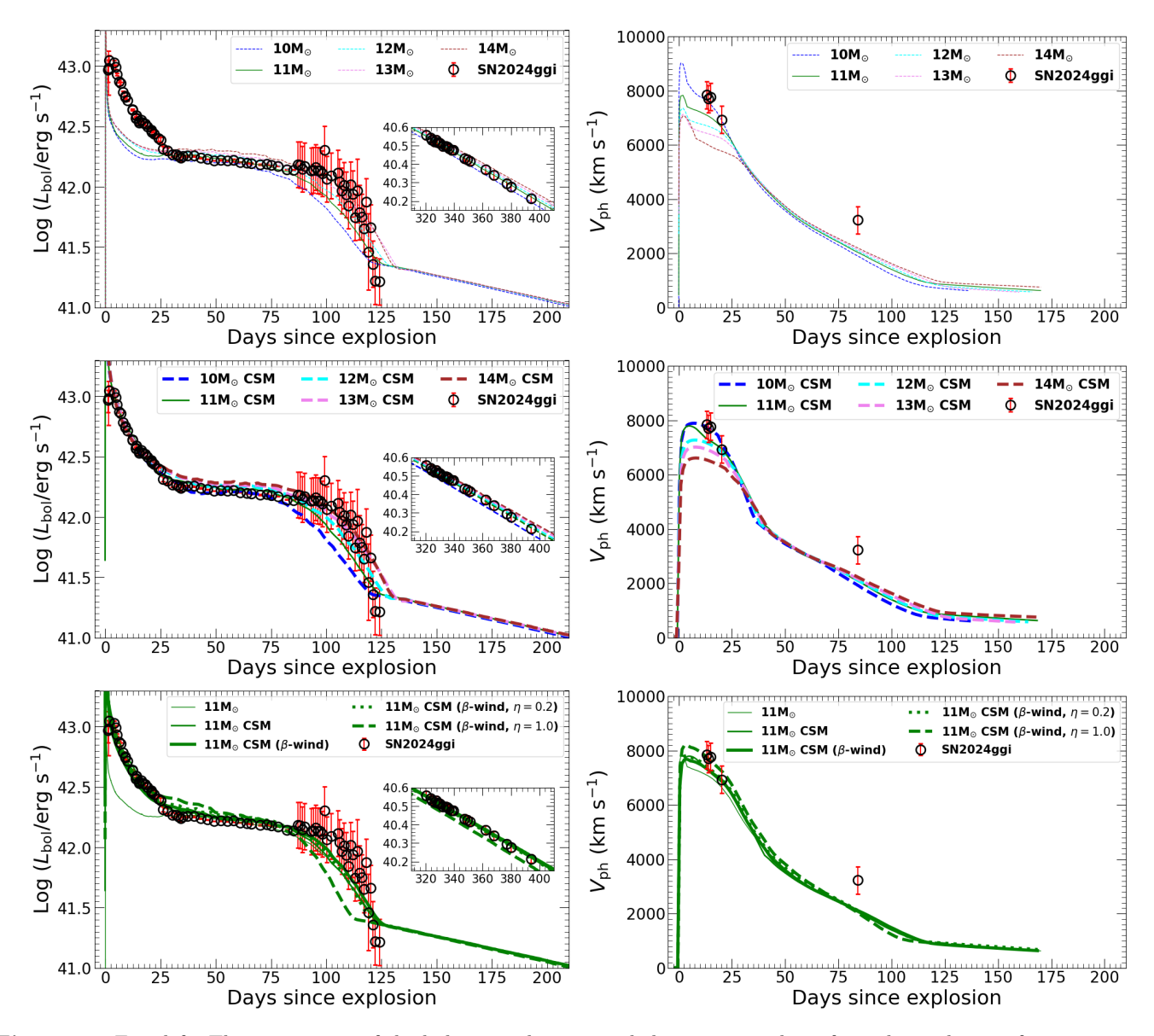


Figure 3. Top, left: The comparison of the bolometric luminosity light curves resulting from the explosion of 10, 11, 12, 13, and $14\,\mathrm{M}_\odot$ ZAMS models with SN 2024ggi. Top, right: Corresponding photospheric velocity evolution comparisons with the Fe II line velocities of SN 2024ggi. The bolometric light curve and Fe II line velocities have been imported from K. Ertini et al. (2025). The explosions for 14 (with 40% rotation), 15, 16, and $17\,\mathrm{M}_\odot$ are not simulated due to their distant position on the HR-diagram from the pre-explosion detected progenitor. M iddle, left: Same as the top, left-hand panel but with a steady-state wind CSM included. M iddle, right: Corresponding photospheric velocity evolution comparisons with the Fe II line velocities of SN 2024ggi. B ottom, left: The comparison of the bolometric luminosity light curves resulting from the explosion of preferred $11\,\mathrm{M}_\odot$ model with steady state wind CSM and also with β -wind CSM. The effect of changing η is also indicated here. B ottom, right: Corresponding photospheric velocity evolution comparisons with the Fe II line velocities of SN 2024ggi. All the models here are computed with $E_{\rm exp} = 0.7 \times 10^{51}$ erg and $M_{\rm Ni} = 0.049\,\mathrm{M}_\odot$ (nicely iterating the nebular phase luminosities as indicated in the insets).

3.1. Constraints on $E_{\rm exp}$, $M_{\rm Ni}$, and $M_{\rm ei}$

Once the models have reached the near SBO stages with desired $E_{\rm exp}$ and $M_{\rm Ni}$, we utilize the radiation hydrodynamics code, STELLA (S. I. Blinnikov et al. 1998; S. Blinnikov et al. 2000; S. Blinnikov & E. Sorokina 2004; S. I. Blinnikov et al. 2006) to compute the bolometric light curve and photospheric velocity evolution. STELLA numerically solves the radiative transfer equations by employing the intensity moment approximation in each frequency bin. In typical MESA applications, it operates with 40 frequency groups, sufficient to generate the spectral energy distributions.

The left-hand side of the top panel of Figure 3 shows the comparison of the STELLA-generated bolometric luminosity light curves from the synthetic explosions of our models with the observed bolometric luminosity light curve, while the top right-hand panel shows the comparison of the STELLA-generated photospheric velocity $(V_{\rm ph})$ evolution with the observed Fe II (5169 Å)-line velocities of SN 2024ggi. The $V_{\rm ph}$ estimated by STELLA at a particular instant is the velocity at the location of the photosphere where the Rosseland optical depth $(\tau_{\rm Ros})$ is 2/3 (B. Paxton et al. 2018). The observed bolometric light curve and Fe II-line velocities are adopted from K. Ertini et al. (2025). The most plausible progenitor having an initial mass of $11 \,\mathrm{M}_{\odot}$ requires $E_{\mathrm{exp}} =$ 0.7×10^{51} erg and $M_{\rm Ni} = 0.049 \, \rm M_{\odot}$ to iterate the observed bolometric light curve (barring the initial ~ 30 days, details about it in the next section) and Fe II velocities. We provide a discussion on the choice of this nickel mass and the consequence of choosing a lower or higher nickel mass in the next section. A recent study by L. Dessart et al. (2025) indicates a slightly larger $M_{\rm Ni}$ of 0.06 ${\rm M}_{\odot}$. However, it is close to the amount $(0.05-0.06\,\mathrm{M}_{\odot})$ obtained by L. Ferrari et al. (2025). The E_{exp} in our modeling seems to be smaller than W. V. Jacobson-Galán et al. (2024); K. Ertini et al. (2025); however, it is in line with the delayed neutrino explosion mechanism of CCSNe as investigated in N. Soker (2024).

In these two subplots, we also see the corresponding results for the 10, 12, 13, and $14\,\mathrm{M}_\odot$ models with similar E_exp and M_Ni . Although all the models seem to explain the observed plateau and the falling tail of SN 2024ggi, only the 10 and $12\,\mathrm{M}_\odot$ models could attain the initial observed Fe II velocities. Thus, our constraint of $11^{+1}_{-1}\,\mathrm{M}_\odot$ on initial progenitor mass further solidifies. The corresponding values of M_ej from the 10, 11, and $12\,\mathrm{M}_\odot$ are $8.2\,\mathrm{M}_\odot$, $9.1\,\mathrm{M}_\odot$, and $9.6\,\mathrm{M}_\odot$, respectively. Thus, we constrain the range of M_ej for SN 2024ggi to be [8.2 – 9.6] M_\odot .

Now, more than a year since the discovery of SN 2024ggi, a few nebular phase spectroscopic observations are also there in the literature. Comparing the molecule-free radiative-transfer model-generated spectra with nebular phase spectroscopy, L. Dessart et al. (2025) constrain an explosion energy and nickel mass of $\sim 10^{51}$ erg and $0.06 \,\mathrm{M}_{\odot}$, respectively. Further, while studying the late-time bolometric light curve, L. Ferrari et al. (2025) propose a nickel mass of $0.05 - 0.06 \,\mathrm{M}_{\odot}$ for SN 2024ggi. The comparisons of the [O I]/[Ca II] flux ratio in the nebular phase spectra with models from A. Jerkstrand et al. (2014) and L. Dessart et al. (2021) reveal a progenitor having initial mass of around $10-12 \,\mathrm{M}_{\odot}$ (L. Ferrari et al. 2025). These observational constraints on nickel mass and initial mass are well in line with our results derived from simulations.

3.2. Constraints on the CSM properties and the effect of variation of $E_{\rm exp}$ and $M_{\rm Ni}$

We see in the previous section that the bolometric luminosities of the initial few days (~ 30 days) can not be reproduced by any of the models. An ad-hoc mechanism of CSM interaction has been proposed to account for the additional luminosities during the initial days of such Type II SNe. The presence of CSM around the SN 2024ggi progenitor has been confirmed by several observations (W. V. Jacobson-Galán et al. 2024; T. Pessi et al. 2024; M. Shrestha et al. 2024; J. Zhang et al. 2024; T.-W. Chen et al. 2025).

To model the CSM around the possible progenitor of SN 2024ggi, we assume steady state wind with velocity, $v_{\rm CSM} = 37 \, \rm km \, s^{-1}$. The choice of this velocity is supported by the value of $37\pm4\,\mathrm{km\,s^{-1}}$ obtained by M. Shrestha et al. (2024) using high-resolution spectroscopic observations during the early phases of SN 2024ggi. For all the models with CSM, we incorporate the wind duration, $t_{\rm CSM} = 0.5\,{\rm yr}$ and mass-loss rate, $\dot{M}_{\rm CSM} = 1.0 \, \rm M_{\odot} \, yr^{-1}$. With the assumed mass-loss rate, the amount of CSM mass (M_{CSM}) around our progenitor models is $\sim 0.5 \, \mathrm{M}_{\odot}$, which is slightly higher than T.-W. Chen et al. (2025) but similar to K. Ertini et al. (2025). For our preferred model having initial mass of $11 \,\mathrm{M}_{\odot}$, the extent of CSM reaches up to $1.2 \times 10^{14} \,\mathrm{cm}$ $(\sim 1660\,\mathrm{R}_{\odot})$. The inferred mass-loss indicates that the progenitor suffered an enhanced mass-loss during the last ~ 180 days before the explosion. We find that the $M_{\rm CSM}$ in our modeling to produce the right amount of CSM responsible for ejecta-CSM interaction is smaller than $\dot{M}_{\rm CSM} = 3.6 \, \rm M_{\odot} \, yr^{-1}$ obtained by K. Ertini et al. (2025) in the steady wind case. The explosion results with steady-wind CSM are shown in the middle panels of Figure 3. It may not be very likely for any RSG star

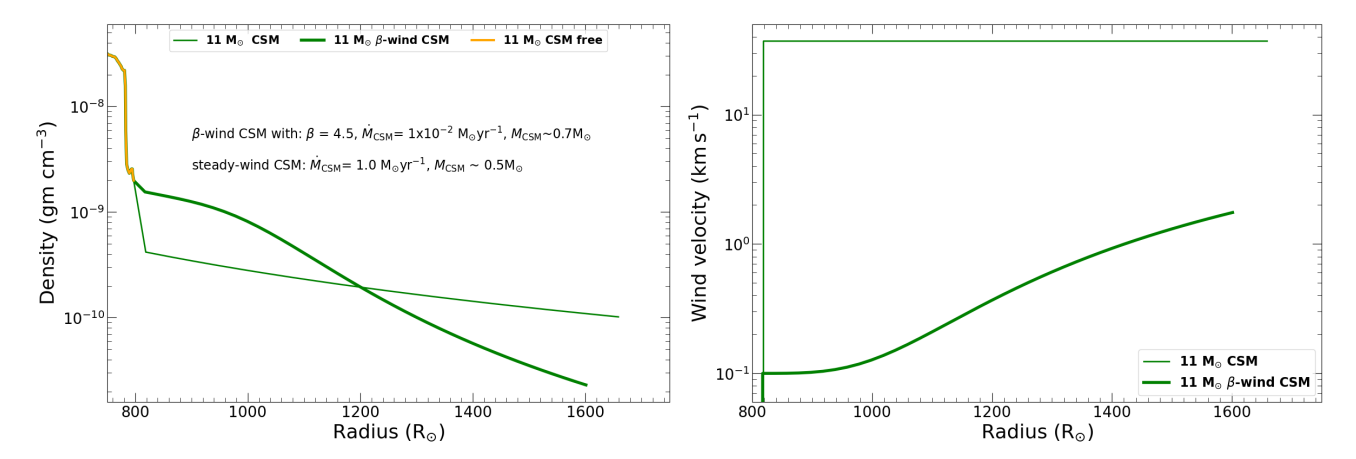


Figure 4. Left: The density distribution as a function of radius for the two different CSM models assumed in the study. Right: Corresponding wind velocity distribution.

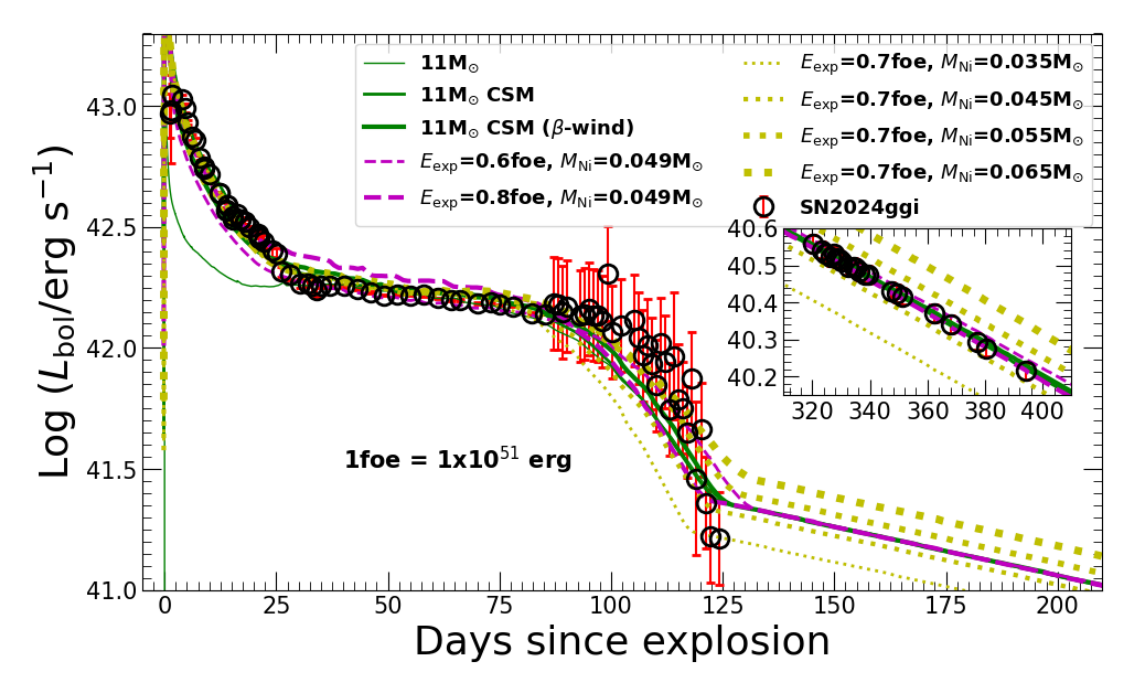


Figure 5. Effect of varying explosion energy and nickel mass on the $11 \,\mathrm{M}_\odot$ model with accelerated-wind CSM (for comparison, the steady-wind CSM model is also shown). The variations help us to constrain the range of plausible explosion energy and the amount of nickel mass.

to have such a high mass-loss rate. As a consequence, we also incorporate the accelerated-wind (also known as the β -wind) scenario as prescribed by T. J. Moriya et al. (2018).

For the accelerated-wind case, we adopt the β velocity law for the wind as mentioned in T. J. Moriya et al. (2018), $v_{\text{CSM}} = v_0 + (v_{\infty} - v_0)(1 - R_0/r)^{\beta}$. Here, v_0 is the initial wind velocity, and it is so chosen that the CSM density is smoothly connected from the surface of the progenitor. R_0 is the radial coordinate where the CSM is attached to the progenitor model. v_{∞} is the terminal wind velocity which is $37 \, \text{km s}^{-1}$ from M. Shrestha et al. (2024). We also use $v_0 = 0.1 \, \text{km s}^{-1}$

(from K. Ertini et al. 2025) and $\beta=4.5$ (accepted values being 1–5, as presented in T. J. Moriya et al. 2018) while modeling the initial stages of SN 2024ggi. We tried different combination of CSM properties, however, the preferred model having initial mass of $11\,\mathrm{M}_\odot$ with accelerated-wind scenario required a mass-loss rate $\dot{M}_{\mathrm{CSM}}=1\times10^{-2}\,\mathrm{M}_\odot\,\mathrm{yr}^{-1}$ with the CSM extended upto $1.1\times10^{14}\,\mathrm{cm}~(\sim1600\,\mathrm{R}_\odot)$. The bottom panels of Figure 3 show the corresponding comparisons of the bolometric light curve (left) and photospheric velocity evolution (right) for the β -wind CSM case. The accelerated-wind mass-loss rate in our case is in line with W. V. Jacobson-Galán et al. (2024); M. Shrestha et al. (2024);

J. Zhang et al. (2024). An amount of $\sim 0.7\,\mathrm{M}_\odot$ is required to explain the initial enhancement in the luminosity. Thus, the accelerated-wind CSM structure requires a slightly higher amount and nearly similar extent of CSM to explain the early enhancement in the luminosity. From the velocity evolution panels in the second column of the Figure 3, we notice that at the early times, the favored models (i.e., the models with $11\,\mathrm{M}_\odot$) show little/no difference between the photospheric velocity and the Fe II line velocities. However, as the photosphere moves deeper into the ejecta, we see that the two velocities start to diverge substantially and the actual measured Fe II velocity point lies slightly higher than the V_ph curve (a well-known behavior mentioned in B. Paxton et al. 2018).

The effect of changing η on the light curve is also shown in the bottom panels of Figure 3. A small increment in η (0.1 to 0.2) has a negligible effect on the light curve shape; however, a large change (0.1 to 1.0) significantly reduces the plateau duration. Due to an increased mass-loss rate, this reduction in plateau duration is attributed to a smaller outer hydrogen envelope, which controls plateau duration. This analysis also rules out the possibility of a much lower (say, $9\,\mathrm{M}_\odot$) initial mass progenitor for SN 2024ggi, as it might not have massive enough hydrogen envelope to explain the observed plateau duration.

To provide a detailed view of the CSM assumed in the present analysis, the density structures of the steadywind and accelerated-wind scenarios are shown in the left-hand panel of Figure 4. The right-hand panel of Figure 4 displays the wind velocity distribution for the two CSM structures. In case of β -wind CSM, the wind velocity near the progenitor star is very small, which smoothly increases as the radius increases; however, in the steady state CSM case, the wind velocity remains fixed to $37 \,\mathrm{km}\,\mathrm{s}^{-1}$ throughout. A recent study by J. T. van Loon (2025) pointed out that RSGs have extended, dense atmospheres from which only a fraction is lost through a stellar wind. The high inferred mass-loss rates in the years preceding an SN explosion likely reflect the dense atmosphere, not a wind, and therefore do not represent mass loss and should instead by quantified in terms of density only.

From the preferred $11\,\mathrm{M}_\odot$ model with accelerated-wind CSM, we try to constrain the E_exp and M_Ni by varying one of these two parameters while keeping the other fixed. As shown in Figure 5, a reduced E_exp of $0.6\times10^{51}\,\mathrm{erg}$ seems to slightly over produce the plateau duration in the observed bolometric luminosity light curve. If we increase the E_exp to $0.8\times10^{51}\,\mathrm{erg}$, the

tail phase improves, although one can notice that the plateau luminosity is increasing. Thus, we can not vary the explosion energy much and provide a range of [0.7– 0.8×10^{51} erg. As shown in Fig. 5, the model with $M_{
m Ni}$ of 0.049 ${
m M}_{\odot}$ nicely iterates the observed luminosities. The amount of the nickel mass absolutely matches to the value estimated by the analytical model fit represented by the equation 1 in L. Ferrari et al. (2025). Further, we see that the models with $M_{\rm Ni} = 0.055\,{\rm M}_{\odot}$ and $0.065\,{\rm M}_{\odot}$ slightly over-estimate the nebular phase lumi-Moreover, a lesser amount $(0.035\,\mathrm{M}_\odot)$ and $0.045 \,\mathrm{M}_{\odot}$) of M_{Ni} underestimates the nebular phase luminosity. Thus, we robustly constrain an amount of $0.049\,\mathrm{M}_\odot$ of nickel synthesized in SN 2024ggi.

4. DISCUSSION AND CONCLUSION

In the current work, we performed detailed hydrodynamic simulations for SN 2024ggi. We started by choosing a range of progenitors having initial masses of $[10\text{--}17]\,M_{\odot}$, evolved them up to their pre-SN stages, and finally simulated their explosions to mimic the observed bolometric light curve and velocity evolution of SN 2024ggi. We utilized one of the most advanced modules, MESA, in conjunction with STELLA to perform the entire simulations.

- Among all the models in our study, the location of $11 \,\mathrm{M}_{\odot}$ at its pre-SN stage on the HR-diagram matched well with the directly detected progenitor candidate in the pre-explosion images. However, we found it difficult to completely rule out the $10 \,\mathrm{M}_{\odot}$ and $12 \,\mathrm{M}_{\odot}$ models due to their proximity to the directly detected progenitor candidate on the HR-diagram. Thus, although the $11\,\mathrm{M}_{\odot}$ progenitor appeared more plausible, we provided a constrain of $11^{+1}_{-1} \,\mathrm{M}_{\odot}$ on the progenitor mass. The pre-SN radius of the preferred $11\,\mathrm{M}_\odot$ model was $800 \,\mathrm{R}_{\odot}$, however, due to the mass constraint obtained, the range of pre-SN radius would be [690] -900 R_{\odot}. These constraints on mass and radius were in line with the observationally estimated values reported in D. Xiang et al. (2024); X. Hong et al. (2024).
- To explain the overall observed bolometric light curve and velocity evolution, the plausible model with an initial mass of $11\,\mathrm{M}_\odot$ required an E_exp of $[0.7\text{--}0.8]\times10^{51}$ erg, M_Ni of $\mathbf{0.049\,M}_\odot$, M_ej of $9.1\,\mathrm{M}_\odot$, and an amount of $\sim0.7\,\mathrm{M}_\odot$ of CSM extended up to $\sim1600\,\mathrm{R}_\odot$ (assuming acceleratedwind CSM). However, due to the constraint of

- $11^{+1}_{-1}\,\mathrm{M}_{\odot}$ on the initial mass, the range of pre-SN radius and ejecta mass would be [690–900] R_{\odot} , and [8.2–9.6] M_{\odot} . The overall pre-SN properties and explosion results for 13 and 14 M_{\odot} models in our simulations disfavored a high mass progenitor for SN 2024ggi.
- Comment on the initial mass degeneracy: While performing hydrodynamic modeling of the Type IIP SNe, J. A. Goldberg & L. Bildsten (2020) indicated initial mass degeneracies. Different initial mass progenitors could produce similar bolometric light curves and velocity evolution from different initial physical conditions (e.g., rotation, massloss, etc.). However, we saw how changing the initial parameters (rotation and eta) in our models impacted their overall evolution and terminating positions on the HR-diagram. In the present study, we had additional informations on the progenitor candidate's luminosity, effective temperature, and mass through pre-explosion progenitor candidate detection. Thus, the preferred initial mass would be the one that lied in the proximity of the position of the pre-explosion detected progenitor candidate on the HR diagram. Ultimately, our constrained progenitor with initial mass of $11^{+1}_{-1} \,\mathrm{M}_{\odot}$ not only matched the position of

the pre-explosion detected progenitor **candidate** on the HR-diagram, but also explained the observed bolometric light curve and velocity evolution satisfactorily.

ACKNOWLEDGMENTS

We thank the anonymous referee for providing constructive comments helpful in improving the manuscript further. AA thanks Prof. Takashi J. Moriya for useful communications. We are thankful to K. Ertini for kindly sharing the bolometric light curve and Fe II line velocity evolution of SN 2024ggi. We are thankful to L. Ferrari for kindly sharing the bolometric data points of the nebular stage. AA and T.-W.C. acknowledge the Yushan Young Fellow Program by the Ministry of Education, Taiwan for the financial support (MOE-111-YSFMS-0008-001-P1). T.-W.C. acknowledges funding from the National Science and Technology Council, Taiwan (NSTC grant 114-2112-M-008-021-MY3) to support GREAT Lab. EH acknowledges the Leverhulme Trust for funding (grant ECF-2024-262). MN is supported by the European Research Council (ERC) under the European Union's Horizon 2020 research and innovation programme (grant agreement No. 948381).

REFERENCES

Aryan, A., Pandey, S. B., Gupta, R., & Ror, A. K. 2023, MNRAS, 521, L17, doi: 10.1093/mnrasl/slad020

Aryan, A., Pandey, S. B., Kumar, A., et al. 2022a, Journal of Astrophysics and Astronomy, 43, 87, doi: 10.1007/s12036-022-09866-z

Aryan, A., Pandey, S. B., Yadav, A. P., et al. 2022b, Journal of Astrophysics and Astronomy, 43, 2, doi: 10.1007/s12036-021-09784-6

Aryan, A., Pandey, S. B., Zheng, W., et al. 2021, MNRAS, 505, 2530, doi: 10.1093/mnras/stab1379

Aryan, A., Pandey, S. B., Zheng, W., et al. 2022c, MNRAS, 517, 1750, doi: 10.1093/mnras/stac2326

Asplund, M., Grevesse, N., Sauval, A. J., & Scott, P. 2009, ARA&A, 47, 481,

doi: 10.1146/annurev.astro.46.060407.145222

Beasor, E. R., Davies, B., Smith, N., et al. 2020, MNRAS, 492, 5994, doi: 10.1093/mnras/staa255

Blinnikov, S., Lundqvist, P., Bartunov, O., Nomoto, K., & Iwamoto, K. 2000, ApJ, 532, 1132, doi: 10.1086/308588 Blinnikov, S., & Sorokina, E. 2004, Ap&SS, 290, 13, doi: 10.1023/B:ASTR.0000022161.03559.42

Blinnikov, S. I., Eastman, R., Bartunov, O. S., Popolitov,
 V. A., & Woosley, S. E. 1998, ApJ, 496, 454,
 doi: 10.1086/305375

Blinnikov, S. I., Röpke, F. K., Sorokina, E. I., et al. 2006, A&A, 453, 229, doi: 10.1051/0004-6361:20054594

Bowman, D. M. 2020, Frontiers in Astronomy and Space Sciences, 7, 70, doi: 10.3389/fspas.2020.578584

Brott, I., de Mink, S. E., Cantiello, M., et al. 2011, A&A, 530, A115, doi: 10.1051/0004-6361/201016113

Chen, T.-W., Yang, S., Srivastav, S., et al. 2025, ApJ, 983, 86, doi: 10.3847/1538-4357/adb428

Chen, X., Kumar, B., Er, X., et al. 2024, ApJL, 971, L2, doi: 10.3847/2041-8213/ad62f7

de Jager, C., Nieuwenhuijzen, H., & van der Hucht, K. A. 1988, A&AS, 72, 259

Dessart, L., Hillier, D. J., Sukhbold, T., Woosley, S. E., & Janka, H. T. 2021, A&A, 652, A64, doi: 10.1051/0004-6361/202140839

- Dessart, L., Kotak, R., Jacobson-Galan, W., et al. 2025, arXiv e-prints, arXiv:2507.05803, doi: 10.48550/arXiv.2507.05803
- Ekström, S., Georgy, C., Eggenberger, P., et al. 2012, A&A, 537, A146, doi: 10.1051/0004-6361/201117751
- Ertini, K., Regna, T. A., Ferrari, L., et al. 2025, arXiv e-prints, arXiv:2503.01577, doi: 10.48550/arXiv.2503.01577
- Farmer, R., Fields, C. E., Petermann, I., et al. 2016, ApJS, 227, 22, doi: 10.3847/1538-4365/227/2/22
- Ferrari, L., Folatelli, G., Ertini, K., et al. 2025, arXiv e-prints, arXiv:2507.22794. https://arxiv.org/abs/2507.22794
- Georgy, C., Ekström, S., Eggenberger, P., et al. 2013, A&A, 558, A103, doi: 10.1051/0004-6361/201322178
- Glebbeek, E., Gaburov, E., de Mink, S. E., Pols, O. R., & Portegies Zwart, S. F. 2009, A&A, 497, 255, doi: 10.1051/0004-6361/200810425
- Goldberg, J. A., & Bildsten, L. 2020, ApJL, 895, L45, doi: 10.3847/2041-8213/ab9300
- Heger, A., & Langer, N. 1998, A&A, 334, 210, doi: 10.48550/arXiv.astro-ph/9803005
- Henyey, L., Vardya, M. S., & Bodenheimer, P. 1965, ApJ, 142, 841, doi: 10.1086/148357
- Herwig, F. 2000, A&A, 360, 952. https://arxiv.org/abs/astro-ph/0007139
- Hong, X., Sun, N.-C., Niu, Z., et al. 2024, ApJL, 977, L50, doi: 10.3847/2041-8213/ad99da
- Hoogendam, W., Auchettl, K., Tucker, M., et al. 2024, Transient Name Server AstroNote, 103, 1
- Hunter, I., Lennon, D. J., Dufton, P. L., et al. 2008, A&A, 479, 541, doi: 10.1051/0004-6361:20078511
- Itagaki, K. 2023, Transient Name Server Discovery Report, 2023-1158, 1
- Jacobson-Galán, W. V., Davis, K. W., Kilpatrick, C. D., et al. 2024, ApJ, 972, 177, doi: 10.3847/1538-4357/ad5c64
- Jerkstrand, A., Smartt, S. J., Fraser, M., et al. 2014, MNRAS, 439, 3694, doi: 10.1093/mnras/stu221
- Jermyn, A. S., Bauer, E. B., Schwab, J., et al. 2023, ApJS, 265, 15, doi: 10.3847/1538-4365/acae8d
- Langer, N., El Eid, M. F., & Fricke, K. J. 1985, A&A, 145, 179
- Maeder, A., & Meynet, G. 2000, ARA&A, 38, 143, doi: 10.1146/annurev.astro.38.1.143
- Maeder, A., & Meynet, G. 2001, A&A, 373, 555, doi: 10.1051/0004-6361:20010596

- Moriya, T. J., Förster, F., Yoon, S.-C., Gräfener, G., & Blinnikov, S. I. 2018, MNRAS, 476, 2840, doi: 10.1093/mnras/sty475
- Nomoto, K., & Hashimoto, M. 1988, PhR, 163, 13, doi: 10.1016/0370-1573(88)90032-4
- Nugis, T., & Lamers, H. J. G. L. M. 2000, A&A, 360, 227
 Ouchi, R., & Maeda, K. 2021, MNRAS, 500, 1889, doi: 10.1093/mnras/staa2527
- Pandey, S. B., Kumar, A., Kumar, B., et al. 2021, MNRAS, 507, 1229, doi: 10.1093/mnras/stab1889
- Paxton, B., Bildsten, L., Dotter, A., et al. 2011, ApJS, 192, 3, doi: 10.1088/0067-0049/192/1/3
- Paxton, B., Cantiello, M., Arras, P., et al. 2013, ApJS, 208, 4, doi: 10.1088/0067-0049/208/1/4
- Paxton, B., Marchant, P., Schwab, J., et al. 2015, ApJS, 220, 15, doi: 10.1088/0067-0049/220/1/15
- Paxton, B., Schwab, J., Bauer, E. B., et al. 2018, ApJS, 234, 34, doi: 10.3847/1538-4365/aaa5a8
- Paxton, B., Smolec, R., Schwab, J., et al. 2019, ApJS, 243, 10, doi: 10.3847/1538-4365/ab2241
- Pessi, T., Cartier, R., Hueichapan, E., et al. 2024, A&A, 688, L28, doi: 10.1051/0004-6361/202450608
- Ror, A. K., Gupta, R., Aryan, A., et al. 2024, ApJ, 971, 163, doi: 10.3847/1538-4357/ad5554
- Shrestha, M., Bostroem, K. A., Sand, D. J., et al. 2024, ApJL, 972, L15, doi: 10.3847/2041-8213/ad6907
- Smartt, S. J. 2009, ARA&A, 47, 63, doi: 10.1146/annurev-astro-082708-101737
- Soker, N. 2024, The Open Journal of Astrophysics, 7, 69, doi: 10.33232/001c.122844
- Srivastav, S., Chen, T. W., Smartt, S. J., et al. 2024, Transient Name Server AstroNote, 100, 1
- Tonry, J., Denneau, L., Weiland, H., et al. 2024, Transient Name Server Discovery Report, 2024-1020, 1
- Van Dyk, S. D. 2017, Supernova Progenitors Observed with HST, ed. A. W. Alsabti & P. Murdin (Cham: Springer International Publishing), 693–719, doi: 10.1007/978-3-319-21846-5_126
- van Loon, J. T. 2025, Galaxies, 13, 72, doi: 10.3390/galaxies13040072
- Vink, J. S., de Koter, A., & Lamers, H. J. G. L. M. 2001, A&A, 369, 574, doi: 10.1051/0004-6361:20010127
- Xiang, D., Mo, J., Wang, X., et al. 2024, ApJL, 969, L15, doi: 10.3847/2041-8213/ad54b3
- Yang, S., Chen, T. W., Stevance, H. F., et al. 2024, Transient Name Server AstroNote, 105, 1
- Zhai, Q., Li, L., Zhang, J., & Wang, X. 2024, Transient Name Server Classification Report, 2024-1031, 1
- Zhang, J., Dessart, L., Wang, X., et al. 2024, ApJL, 970, L18, doi: 10.3847/2041-8213/ad5da4